ACCSCIENCE PUBLISHING

Materials Science in Additive Manufacturing

ORIGINAL RESEARCH ARTICLE

Laser powder bed fusion of atomized industrial waste-derived Inconel 725 alloy powders: A machine learning-assisted process optimization

Gabriele Locatelli*, Sara Bocchi, Mariangela Quarto, and Gianluca D'Urso

Department of Management, Information and Production Engineering, University of Bergamo, Bergamo, Lombardy, Italy

Abstract

Among nickel-based superalloys, Inconel® 725 (IN725) stands out for its excellent strength and corrosion resistance. Despite this, its application in additive manufacturing remains largely unexplored. This study investigates laser powder bed fusion of metals (PBF-LB/M) applied to IN725 powder derived from recycled industrial waste, addressing sustainability and process optimization goals. Using the design of experiments approach, the laser power–scan speed process parameter space was explored. Gaussian process regression models were developed to predict surface roughness, relative density, and microhardness. Both direct process parameters and volumetric energy density were evaluated as model inputs to assess predictive performance. The findings established a broad optimal process window for manufacturing high-quality IN725 parts using PBF-LB/M. Specifically, an optimal combination of 99.99% relative density, 7.3 μm roughness, and 311 HV microhardness was achieved by processing the powder at 250 W and 1,500 mm/s. By demonstrating the feasibility of using recycled IN725 powder, this study contributes to the development of sustainable manufacturing practices and supports wider adoption of PBF-LB/M in oil and gas, marine, and chemical processing industries, where IN725 is widely employed.

Keywords: Powder bed fusion; Inconel 725; Waste recycling; Process optimization; Machine learning

***Corresponding author:**
Gabriele Locatelli
(gabriele.locatelli@unibg.it)

Citation: Locatelli G, Bocchi S, Quarto M, D'Urso G. Laser powder bed fusion of atomized industrial waste-derived Inconel 725 alloy powders: A machine learning-assisted process optimization. *Mater Sci Add Manuf*. 2026;5(1):025320072. doi: 10.36922/MSAM025320072

Received: August 06, 2025

Revised: September 02, 2025

Accepted: September 10, 2025

Published online: November 5, 2025

1. Introduction

Nickel-based superalloys are high-performing materials renowned for combining exceptional mechanical strength and toughness with high resistance to corrosion and oxidation, properties that are maintained at temperatures up to 1,000°C.[1] Due to these properties, nickel-based superalloys have been extensively employed in the fabrication of components operating in safety-critical applications, including aerospace, power generation, and chemical processing industries.[2,3] Despite their outstanding performance in critical environments, nickel-based superalloys are also considered difficult-to-machine materials. Work hardening, high melting points, and low thermal

conductivity result in high cutting temperatures and a fast tool wear rate.[4,5]

In the last decade, laser powder bed fusion of metals (PBF-LB/M) has emerged as a valuable alternative for manufacturing nickel-based superalloy components, due to its potential in enhancing mechanical properties by optimizing microstructure formation.[6] Furthermore, PBF-LB/M offers the possibility to produce complex geometries and enable design flexibility that goes beyond conventional manufacturing constraints, as fine layers of metal powder are selectively melted by a laser beam, according to a three-dimensional model, until parts are completed.[7,8]

Since the laser–powder interaction in the PBF-LB/M process causes rapid localized melting and high thermal gradients, the metal weldability is regarded as a useful indicator in determining the challenge rate for manufacturing parts with acceptable integrity.[9] Among nickel-based superalloys, nickel-chromium Inconel® 625 (IN625) and 718 (IN718) alloys have garnered substantial attention in the context of PBF-LB/M, due to their excellent weldability and favorable response to this additive manufacturing technique.[10,11] IN625 is a solid-solution strengthened alloy that exhibits superior corrosion resistance and thermal fatigue performance, especially in marine and chemical environments, and is generally easier to process via PBF-LB/M due to its lower susceptibility to hot cracking and segregation phenomena during solidification.[12] IN718 is a precipitation-hardened alloy that excels in the fabrication of aerospace components and gas turbines, given that it can maintain excellent creep resistance and high strength at elevated temperatures, up to approximately 650°C.[13] Due to the possibility of achieving unprecedented property tuning through tailored microstructure adjustments and process parameter optimization,[6,14] PBF-LB/M processing holds potential for adapting several other commercial superalloys. In addition to the well-established IN718 and IN625, research has been increasingly focused on more complex alloys such as IN738 and IN939, which offer superior high-temperature performance but pose difficulties during processing due to their high gamma prime content and crack sensitivity.[15-17] To a minor extent, other high-performance superalloys are at the center of research efforts for PBF-LB/M production, including Hastelloy X, René 80, Haynes 230, and Nimonic 263.[18-21]

In the wake of the growing interest in extending PBF-LB/M processing to a wider portfolio of superalloys, the nickel-chromium-molybdenum-niobium alloy IN725 emerges as a suitable candidate, as it was developed to combine the high strength of IN718 with the excellent corrosion resistance of IN625.[22] In particular, the high molybdenum content contributes to superior corrosion resistance in sour brine and high-temperature environments, making IN725 particularly attractive for applications in the oil and gas, marine, and nuclear industries.[23] The ability of PBF-LB/M to produce complex geometries and reduce lead times could position IN725 as a strategic alloy for future additive manufacturing-driven innovation in these sectors. Despite the promising premises for IN725, only one study has investigated its feasibility for laser powder bed fusion manufacturing. Todaro *et al.*[24] demonstrated for the 1st time the printability of IN725 with PBF-LB/M using thermodynamic and metallurgical analyses, confirming the low susceptibility of IN725 to solidification and strain–age cracking, highlighting its excellent printability compared to other high-strength superalloys. Todaro *et al.*[24] also demonstrated that the alloy can be processed with a crack-free and near-pore-free microstructure across a wide process parameter window, achieving relative densities up to 99.6% through laser scan speed and hatch spacing optimization. The present study builds on the early work of Todaro. While that work represents a fundamental reference for the preliminary validation of the material, the approach adopted here focuses on systematically optimizing the printing process through predictive modeling based on machine learning (ML) techniques. This study extends the investigation of IN725 manufactured by PBF-LB/M to include powders recycled from industrial waste, thereby contributing to a sustainable approach.

Accurate and reliable models that relate the process parameters to their properties are required to perform an effective optimization. Numerical modeling efforts at multiple length scales in additive manufacturing can provide the input-output relation needed for process optimization with high accuracy. However, high computational times and costs make numerical models unsuitable for optimization studies.[25] Therefore, experimental optimization coupled with simplified statistical models is still commonly performed. Due to the complexity of additive manufacturing processes, ML has emerged as a valuable tool for identifying process–structure–property relations while providing sufficiently accurate predictions for optimization. Neural network methods are preferred for high-dimensional datasets, while data-driven methods typically perform better when less training data is available.[26]

The process optimization was conducted by combining a design of experiments (DoE) approach with Gaussian process regression (GPR) models to model the relationship between process parameters and product outputs (e.g., surface roughness, relative density, and microhardness).

The use of recycled powders promotes closed-loop material flows and reduces carbon dioxide emissions compared to the atomization of fresh powders,[27] promoting the adoption of sustainable manufacturing and industrial ecology practice.[28] A DoE was employed to explore and optimize the laser power–scan speed parameter space, as these input variables are the most critical in laser powder bed fusion. GPR modeling was selected among ML algorithms due to its suitability for small datasets and its ability to quantify predictive uncertainty,[29,30] which are essential features for guiding the selection of suitable models for PBF-LB/M.[31] GPR has emerged as a valuable tool for exploring and exploiting scenarios in metal additive manufacturing, as it allows the identification of optimal process windows and a deeper understanding of process–structure–property relations. Lee *et al.*[32] developed a GPR optimization model to enhance the productivity and quality metrics in wire-arc additive manufacturing.[32] Liu *et al.*[26] and Li *et al.*[33] were able to define optimized process windows for the PBF-LB/M processing of AlSi10Mg[26] and CoCrMo alloy,[33] respectively. Similarly, Maitra *et al.*[34] used GPR to predict the density of Ti6Al4V parts.

In this study, GPR models were trained using both direct process parameters (laser power and scan speed) and the volumetric energy density (VED) to draw a comparison based on predictive accuracy. The reliability of VED as a predictor for part quality is debated, as it fails to account for unequal contributions and interaction effects of individual parameters.[35] This study provides a solid foundation for the sustainable adoption of PBF-LB/M in industrial sectors that utilize IN725, while informing future efforts in model selection, parameter optimization, and the adaptation of high-performance superalloys for additive manufacturing. In summary, this work defines an optimal process window for producing dense, smooth, and hard parts, and further compares the effectiveness of direct parameters against those based on VED.

2. Materials and methods

2.1. Powder feedstock

The material used in this study is IN725 recycled powder, supplied by Politecnico di Torino (Italy) after the vacuum inert gas atomization of waste materials. Specifically, the waste materials consisted of UNS N07725 turbine blades, which had been discarded after reaching their end-of-life stage. Detailed information regarding the vacuum inert gas atomization setup used for waste material atomization can be found in the study of Gobber *et al.*[36] As shown in Table 1, the chemical composition of the recycled alloy complies with the American Society for Testing and Materials (ASTM) B805 standard for UNS N07725.[37] The measured oxygen content was 0.00824 ± 0.0016%, well below the 0.3% threshold set as an indicative maximum limit for PBF processing of IN718.[38] The powder exhibited excellent sphericity, as observed in the micrograph reported in Figure 1A, with smooth particle surfaces and small satellites surrounding the larger particles. The particle size distribution was characterized by D_{10} = 21.3 µm, D_{50} = 42.4 µm, and D_{90} = 68.0 µm (Figure 1B). The flowability and apparent density of the powder batch, measured using a Hall flowmeter funnel, according to ASTM B213 and B212 standards,[39,40] were 10.50 ± 0.20s and 4.69 ± 0.007 g/cm^3, respectively. The morphological and physical characteristics of the powder were compatible with PBF-LB/M processing, confirming the suitability of recycled material to be used in additive manufacturing, despite being derived from end-of-life components.

2.2. Sample fabrication

To optimize the PBF-LB/M process, a full factorial DoE was defined to vary laser power (P) and scan speed (v) within the ranges of 100–300 W and 500– 00 mm/s, respectively, as these parameters exert a dominant influence on melt pool behavior, defect formation, and microstructural evolution.[41,42] In contrast, hatch distance (h) and powder layer thickness (t) were held constant, as their effects can be considered secondary during initial process window development.[43] The powder layer thickness was kept constant at 30 µm. Due to the lack of knowledge on the PBF-LB/M-processed IN725, hatch distance was set to 50 µm, a value previously shown to enhance part densification while mitigating excessive surface roughness associated with particle adhesion in other alloys.[44,45] The 20 parameter combinations resulting from the DoE are summarized in Table 2, and the corresponding VEDs were calculated according to Equation I:

$$VED = \frac{P}{v.h.t} \quad (I)$$

Table 1. Chemical composition of the Inconel 725 recycled powder (wt%)

Element	Nickel	Chromium	Molybdenum	Niobium	Titanium	Aluminum	Carbon	Sulfur	Iron
This study	57.45	21.25	7.86	3.40	1.65	0.29	0.008	0.00042	7.95
ASTM B805[37]	55–59	19–22.5	7–9.5	2.75–4	1–1.7	≤0.35	<0.03	<0.015	Balance

Abbreviation: ASTM: American society for testing and materials.

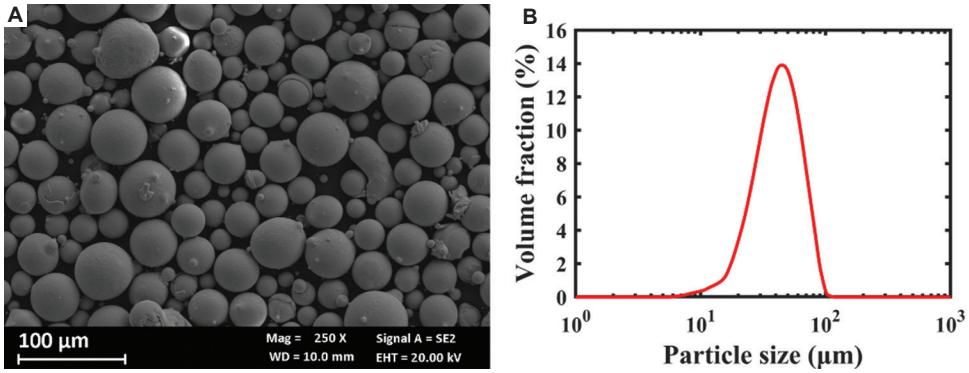

Figure 1. Inconel 725 recycled powder. (A) Scanning electron microscopy morphology. Scale bar: 100 µm; magnification: ×250. (B) Particle size distribution.

Table 2. Laser powder bed fusion process parameters used for the design of experiments

Sample	Laser power (W)	Scan speed (mm/s)	Volumetric energy density (Jmm^3)
1	100	500	133
2	100	1,000	66
3	100	1,500	44
4	100	2,000	33
5	150	500	200
6	150	1,000	100
7	150	1,500	67
8	150	2,000	50
9	200	500	267
10	200	1,000	133
11	200	1,500	89
12	200	2,000	667
13	250	500	333
14	250	1,000	167
15	250	1,500	111
16	250	2,000	83
17	300	500	400
18	300	1,000	200
19	300	1,500	133
20	300	2,000	100

A total of 20 cylindrical samples with 10 mm diameter and 6 mm height (Figure 2) were fabricated using a Print Genius 150 machine by Prima Additive S.r.l. (Italy). The machine has a 300 W ytterbium-fiber laser operating at a 1,070 nm continuous wavelength. All samples were fabricated using a 5 mm stripe pattern scanning strategy with a 67° counter-clockwise rotation between layers. The diameter of the laser spot was set to 100 µm. The build plate was preheated to 80°C to stabilize melt pools and ensure consistent melting and structural integrity of the initial layers, which are crucial for promoting successful adhesion between the substrate and the part.[46] High-purity argon was used as the shielding gas, keeping the oxygen level inside the build chamber below 0.1%, to avoid alloy oxidation during printing.

2.3. Characterization of surface roughness, relative density, and hardness

All the samples produced in this study were measured and tested in their as-built condition, without undergoing post-processing or post-heat treatment. After removing the build plate from the PBF-LB/M machine, the samples were cut using wire electrical discharge machining.

The surface roughness of all samples was measured using a Sensofar S-Neox optical profilometer (Sensofar metrology, Spain) utilizing the focus variation technique. All measurements were conducted with 10× magnification at the same region of interest locations over a 1,754.40 × 1,320.96 mm^2 area.

Microhardness was measured using a UHL VMH-001 Vickers hardness tester (Uhl technische Mikroskopie GmbH, Germany). Before testing, the top surface of all samples was polished up to a 1 µm surface finish. Four HV_{1000} indentations were performed on each sample under a 1,000 gf load applied for 15 s, according to the ASTM E384 standard,[47] and measured with a ×50 objective lens.

The specimens were then cut parallel to the build direction, mounted in phenolic resin, ground according to a sequence of 120, 180, 400, 1,200, 2,400, and 4,000 grit SiC emery paper, and polished using 3 µm diamond suspension. Micrographs of ×200 magnification were taken to cover the cross-section and stitched together using a Keyence VHX-7100 optical microscope (Keyence Corp., Japan). The ImageJ software ((version 1.54g); National Institutes of Health, United States)) was then used to measure porosity after binarization of the micrographs, following the pipeline detailed in a previous work.[48]

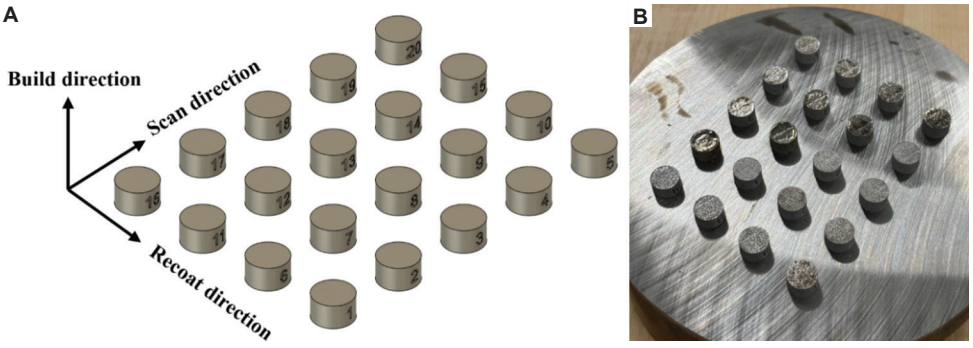

Figure 2. Sample layouts. Layout of the (A) as-designed and (B) as-printed cylindrical samples.

2.4. GPR

The GPR was used to model the relationship between the PBF-LB/M process parameters and the tested output properties of the IN725 alloy samples. The dataset comprised all data acquired during the experimental campaign based on the full factorial DoE. It represents the PBF-LB/M process, covering diverse processing conditions ranging from low to high energy density regimes.

GPR is a non-parametric, supervised ML algorithm that relies on Bayesian inference to learn the relationship between inputs and outputs that most likely generated a dataset, letting the data determine the level of complexity.[49] Since the Bayesian framework does not assume a fixed functional form, GPR yields robust predictions even with limited datasets.[50] Specifically, GPR draws the input-output relation from a Gaussian process with mean function μ and covariance function *k*, as per Equation II:

$$Y(x) = GP(\mu(x), k(x, x')) \quad \text{(II)}$$

Where *y* denotes the output variable, while x and x' represent the training and prediction input variables, respectively.

In this study, GPR was utilized to map the relationship between relative density (ρ), surface roughness (*Sa*), and microhardness (HV_{1000}) of IN725 alloy samples with two different sets of input variables. In the first case, laser power (*P*) and scan velocity (*v*) inputs were considered, while VED was used as the only input variable in the second case, as expressed in Equations III and IV:

$$\rho \mid Sa \mid HV_{1000}(P,v) = GP(\mu(P,v), k(P,v,P', v')) \quad \text{(III)}$$

$$(\rho \mid Sa \mid HV_{1000}(VED) = GP(\mu(VED), k(VED, VED')) \quad \text{(IV)}$$

Before training the models, min-max and z-score normalizations were applied to remove measurement scales from the input and output data. Regardless of the adopted ML approach, this preprocessing step facilitates model training and improves accuracy.[51] Since no strong prior trend is known, the models were trained assuming a zero-mean function (μ = 0). The covariance function was instead defined through a Matérn 5/2 kernel with automatic relevance determination (ARD-Matèrn 5/2). This kernel function was chosen because it is suited to model various spatial correlation structures while considering a separate length scale for each predictor.[52,53] Furthermore, the ARD-Matèrn 5/2 offers robust and accurate predictions of complex relationships.[54,55] The GPR models were trained in MATLAB (version R2024a) using the fitrgp function. Kernel hyperparameters (i.e., length scales, process variance, and noise variance) were tuned by maximizing the marginal log-likelihood using the built-in quasi-Newton solver, with default settings for convergence tolerances and maximum iterations.

No explicit resampling-based validation was performed, as the probabilistic nature of GPR intrinsically provides predictive variances alongside mean estimates. Hence, the full experimental dataset was used as the training dataset to generate input weights and facilitate the exploration of process–structure–property relationships. For each model, the predictive mean and standard deviation estimated by the GPR were used to plot the response surface and uncertainty map, after mapping results to physical units through inverse z-score transformation. Uncertainty maps served as internal validation to assess the reliability of the predicted response surfaces.

To quantitatively estimate the goodness-of-fit and absolute discrepancies in each model, the coefficient of determination (R^2) and the mean absolute error (MAE) were used as evaluation metrics. R^2 is well-established in regression analysis as it quantifies the proportion of variance in the output variable explained by the model, thus providing an intuitive measure of the overall goodness-of-fit.[56] Complementarily, MAE offers a scale-preserving indicator of average prediction error that is less sensitive to outliers than metrics such as root mean square error, making it particularly suitable for small experimental datasets.[57]

3. Results and discussion

3.1. Surface roughness determination

Figure 3A shows a general trend as surface roughness decreases when the power input increases. However, the magnitude and consistency of this trend varied depending on the specific scan speed value. Concurrently, surface roughness also appeared to generally coarsen when the scan speed used for processing was increased with equal laser power. Interestingly, samples fabricated with a scan speed equal to 1,500 mm/s showed a peculiar trend in which the surface finish strongly improved from 15.67 to 8.93 µm in the 150–250 W range and then stabilized when a 300 W power was used. Furthermore, the experimental data highlight that surface roughness values stabilize when 150 W power is exceeded. This plateau supports the hypothesis that while increasing power improves surface finish, the benefits diminish at high scan speeds.

Figure 3B shows the optical micrographs of characteristics of IN725 alloy surfaces, revealing the presence of spherical particles (indicated by white arrows) that adhered to track segments independently of the PBF-LB/M processing condition. This defect can be attributed to spheroidization, a phenomenon that occurs when molten metal is accelerated into the gas environment due to the Rayleigh–Taylor instability.[58] Under such conditions, surface tension leads to the fragmentation and rounding of elongated melt tracks into small spherical particles towards the edges of melt pools.[59] The consistent observation of such particles despite varying grades of surface roughness suggests that spheroidization is intrinsic to the dynamics of laser–powder interaction in the PBF-LB/M process.

3.2. Relative density analysis

Figure 4A shows that relative density was largely independent of scan speed in the 200–300 W laser power range, indicating that high power ensures complete melting and consolidation under higher scan speeds, as observed in Figure 4B. However, the trend slightly deteriorated under high power-low speed combinations due to excessive energy input, increasing the chance of keyhole formation, as observed in Figure 4C. A contrasting behavior was observed at lower laser powers (100–150 W), where increasing the scan speed generally led to a significant reduction in relative density. The underexposure of the powder bed at lower power inputs resulted in poor interlayer bonding and severe lack-of-fusion formation, as depicted in Figure 4D. Overall, 13 parameter combinations resulted in relative density values exceeding 99.5%, thus identifying a robust process window for near-pore-free fabrication of IN725 via PBF-LB/M. In particular, the highest density achieved in this study, 99.99%, was achieved at 250 W and 1,500 mm/s, corresponding to a VED of 167 J/mm^3.

3.3. Microhardness analysis

Figure 5 shows that microhardness stabilized when the laser power exceeded 200 W and the scan speed was higher than 1,000 mm/s. The relatively uniform values in this region suggest that a stable process regime was achieved, in which balanced energy input and rapid solidification rates promote consistent microstructural characteristics. In contrast, microhardness fluctuated noticeably across the entire power range at 500 mm/s, suggesting excessive energy inputs led to melt pool instabilities that unpredictably affected the final microstructure. The PBF-LB/M process achieved microhardness values that compare favorably with the 300 HV reported for annealed, heat-treated IN725 rods.[60]

3.4. Accuracy evaluation of GPR models

While VED provides a convenient scalar representation of the process energy input, the model evaluation metrics

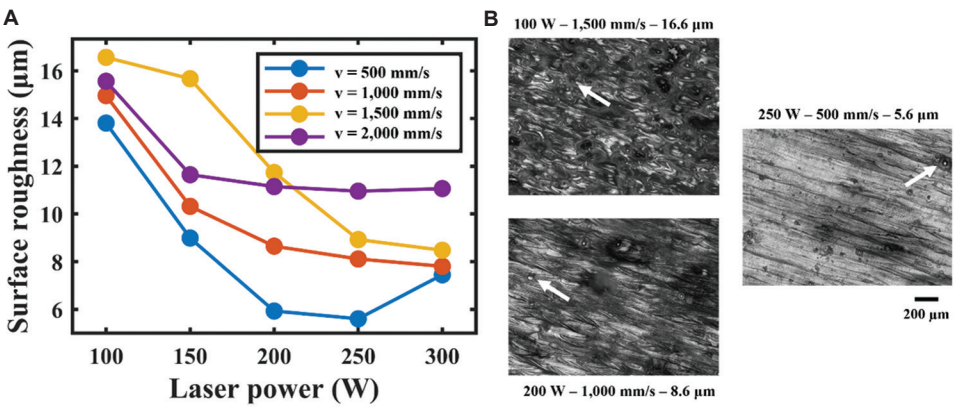

Figure 3. Surface roughness. (A) The relationships between surface roughness and laser power under different scan speed conditions, (B) Optical micrographs of characteristic samples showing surface morphology affected by spheroidization. Scale bar: 200 µm, magnification: ×10.

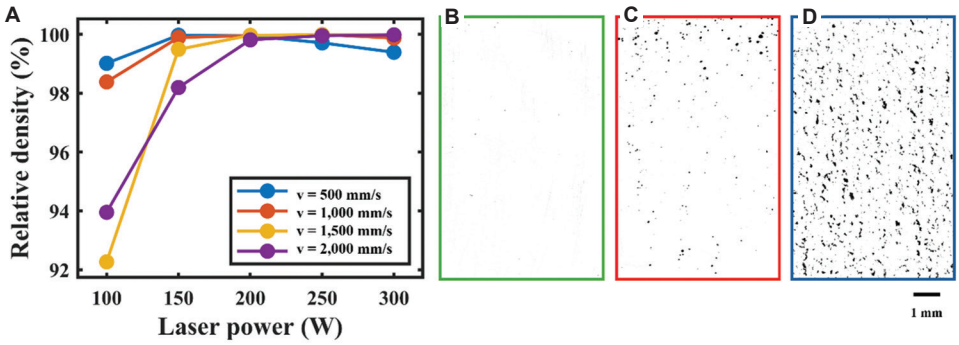

Figure 4. Relative density. (A) The relationships between relative density and laser power under different scan speed conditions. (B-D) Binarized optical images by ImageJ showing characteristic samples with (B) near-pore-free microstructure (p=250 W, *v* = 1,000 mm/s), (C) keyhole pores (p=300 W, *v* = 500 mm/s), and (D) lack-of-fusion pores (p=100 W, *v* = 1,500 mm/s). Scale bar: 1 mm; magnification: ×200.
Abbreviations: *P*: Laser power; *v*: Scan velocity.

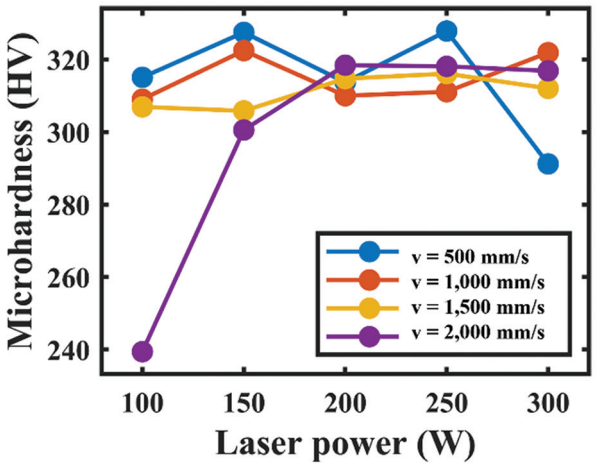

Figure 5. The relationship between microhardness and laser power under different scan speed conditions

Table 3. Evaluation metrics used to assess the accuracy of the Gaussian process regression models

Output variable	Input variable (s)	R^2	Mean absolute error
Relative density (ρ)	*P*, *v*	0.95	0.09%
	VED	0.82	0.24%
Surface roughness (*Sa*)	*P*, *v*	0.99	0.07 μm
	VED	0.73	0.42 μm
Microhardness ($HV_{1,000}$)	*P*, *v*	0.62	0.37 HV
	VED	0.98	0.10 HV

Abbreviations: *P*: Laser power; *v*: Scan velocity; VED: Volumetric energy density.

in Table 3 underline that its use in PBF-LB/M process modeling and optimization is significantly output-dependent. The relative density and surface roughness models trained using laser power and scan velocity as process inputs outperformed those based on VED, achieving higher goodness-of-fit and lower prediction errors. According to widely accepted guidelines,[56] R^2 values in the range of 0.7–0.9 are considered indicative of a good model fit. Hence, while the 0.82 and 0.73 R^2 values achieved in this study support the reliability of using VED as a predictor for process windows achieving high density and low surface roughness in PBF-LB/M, it is clear that these values are not capable of capturing the complexities of laser–powder interactions sensitive to the interplay between laser power and scan speed. Different parameter combinations may yield the same VED value but still result in different microstructures, porosity distributions, and thermal histories.[35] This outcome can be explained by VED condensing multiple parameters into a single scalar, thus neglecting the distinct influence of laser power and scan speed on melt pool dynamics. Different parameter combinations may yield identical VED. However, other dynamics and thermal histories may have characterized the resulting melt pools.

In contrast, microhardness appears to correlate more strongly with cumulative energy input. The VED-based model for microhardness achieved an excellent performance, with an R^2 of 0.98 and an MAE of just 0.10 HV, confirming that VED is a highly effective predictor for this specific output. However, the model trained on laser power and scan speed yielded a remarkably low MAE of 0.37 HV despite achieving a lower R^2 of 0.62. Therefore, the model can be considered highly reliable for practical applications, particularly in contexts where precise point-wise estimation is more critical than explaining the full variance of the data. Furthermore, this result supports the hypothesis that hardness is less sensitive to variations in specific parameter combinations, provided the overall energy density remains constant.[61,62]

Based on this comparative analysis, only GPR models using laser power and scan speed as inputs were considered for optimizing the PBF-LB/M processing of IN725.

3.5. GPR models with laser power and scan speed inputs

Figures 6-8 show the point-wise predictions made by the GPR models, along with corresponding prediction errors, for surface roughness, relative density, and microhardness, respectively. Distinct colors were used to address variations in the predicted outputs and standard deviations, while black dots mark the experimental data entries.

Figure 6A illustrates the response surface predicted by the GPR surface roughness model, indicating that surface finish progressively coarsens as the scanning speed increases and the laser power diminishes. However, laser power appears to substantially influence surface roughness more than scan speed. The model predicted that lower surface roughness is generally achieved at high laser power, regardless of the scan speed. Considering surface roughness ≤10 μm to be a suitable range for acceptable as-built surface roughness, the response surface suggests that optimal parameter combinations can be found at medium-to-high laser power (200–300 W) and low scan speed (500–1,000 mm/s). Figure 6B shows the standard deviations in the surface roughness predictions, identifying higher uncertainty where the model interpolates between sparse data points along the scan speed axis. This behavior indicates that the GPR model for surface roughness is more sensitive to scan speed. Notably, peaks are localized at the boundary of the dataset, thus indicating edge extrapolation errors.

In Figure 7A, the predicted relative density response surface identifies a wide and well-bounded process window for fabricating near-defect-free parts. In particular, parts with relative density ≥99.5% appeared to be preferentially achieved by combinations of medium-to-high laser power ($P \geq 150$) and medium-to-high scan speed ($v \geq 1000$). The plot suggests that the individual input parameters have limited influence on the density percentage of as-built parts, with the relative density predicted to decrease when increasing the scan speed and reducing the laser power concurrently. This behavior enabled the identification of the process window region, resulting in the formation of lack-of-fusion pores, as observed in Figure 4D, which

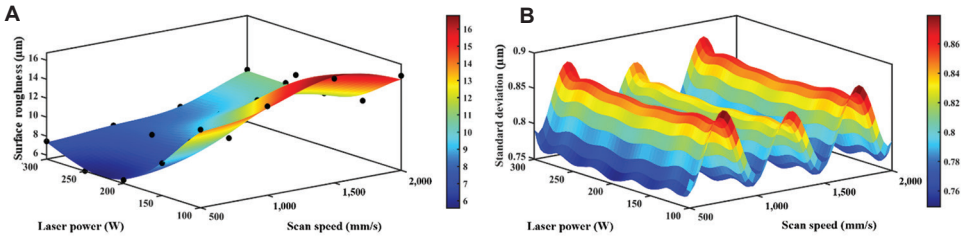

Figure 6. Surface roughness of Gaussian process regression models. (A) Predicted response surface and (B) predicted error surface.

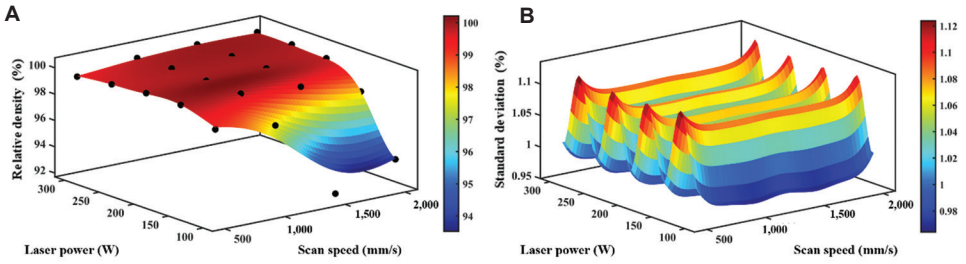

Figure 7. Relative density Gaussian process regression model results. (A) Predicted response surface and (B) predicted error surface.

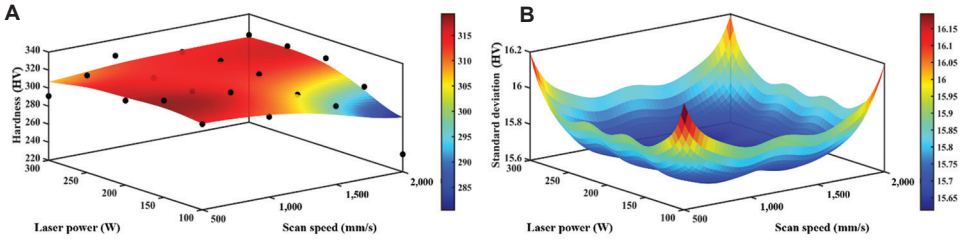

Figure 8. Microhardness of Gaussian process regression models. (A) Predicted response surface and (B) predicted error surface.

typically arise under insufficient melting due to higher scan speed and reduced power.[63] At a high power and low scan speed, the response surface identified a small region where the relative density decreased. Considering the sample printed under the corresponding input parameters (laser power = 300 W and scan speed = 500 mm/s) showed a sub-optimal microstructure characterized by keyhole porosities (Figure 4C), the response surface suggests that reducing the scan speed below 500 mm/s under medium-high laser power would exacerbate keyholing. High power-low velocity combinations result in excessive energy inputs, driving pore formation due to the periodic collapse of keyholes under intense recoil pressure.[63] The standard deviation surface in Figure 7B is consistent with the one presented in Figure 6A, albeit with the highest uncertainty identified along the laser power axis. This indicates that the relative density model is more sensitive to laser power. Again, peaks localized at the boundaries stem from edge extrapolation errors.

In Figure 8A, the predicted response surface clearly illustrates that microhardness tends to decrease as the scan speed increases and the laser power decreases. However, the GPR model predicts that the opposite processing condition also decreases Vickers microhardness progressively as the laser power exceeds 300 W and the scan speed is reduced below 500 mm/s. The observed behaviors are compatible with the trends predicted by the relative density response surface (Figure 7A), indicating that the achievable microhardness is strongly related to the extent of microstructural defect formation disrupting the densification of as-built IN725 parts. The standard deviation surface in Figure 8B shows localized peaks only at the four corners of the dataset, hinting at extrapolation errors. However, the flat surface at the center of the dataset space indicates that the microhardness GPR model is equally sensitive to both laser power and scan speed.

The GPR models are intended to describe parameter–process–property relationships within the investigated parameter space, where their predictions are most reliable. The increased predictive variance values at dataset boundaries highlight reduced confidence outside this range, confirming that the models should not be extrapolated but used primarily for mapping the explored process window.

3.6. Optimal process window

Figure 9 shows the laser power–scan speed process map for PBF-LB/M of the IN725 alloy, derived from the response surfaces of the GPR models in Figures 6A, 7A, and 8A. The predicted contour lines for surface roughness, relative density, and Vickers microhardness are plotted in red, blue, and green, respectively. Energy density contour lines are plotted in black. The light-yellow area in the plot identifies the optimal process window for fabricating IN725 parts with surface roughness ≤10 μm, relative density ≥99.5%, and microhardness ≥300 HV. Within the window, the red star marks the sample produced using 250 W laser power and 1,000 mm/s scan speed, which yielded the most optimal

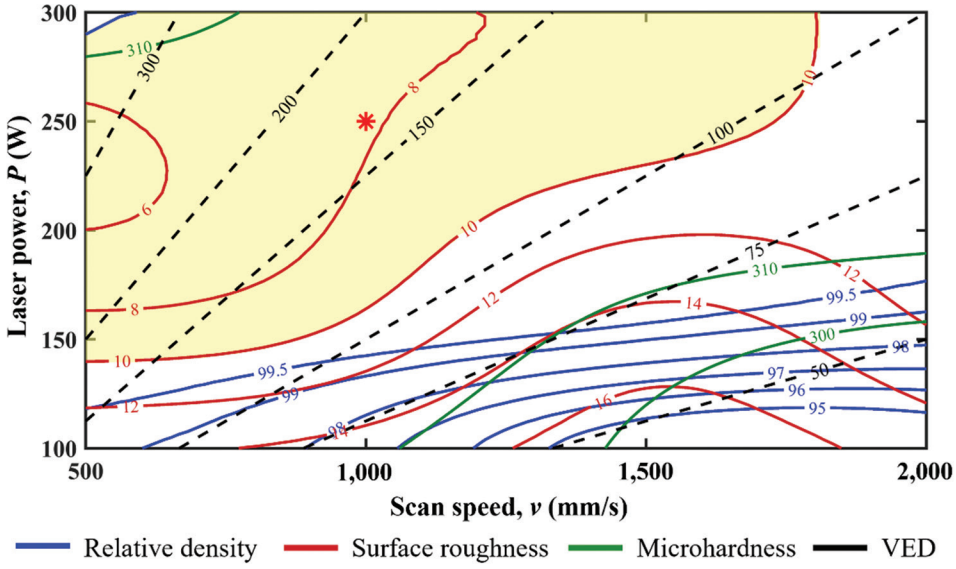

Figure 9. Laser power–scan speed process window based on Gaussian process regression models. The blue, red, and green lines represent relative density, surface roughness, and microhardness contours, respectively. The light yellow area highlights the predicted window to achieve near-pore-free parts with surface roughness ≤10 μm and microhardness ≥300 HV. The black dashed lines represent the VED contour lines. The red star indicates the optimal sample achieved in this study (relative density = 99.5%, surface roughness = 7.3 μm, and microhardness = 311 HV).

build with relative density = 99.5%, surface roughness = 7.3 μm, and microhardness = 311 HV. The process map in Figure 9 indicates that the optimal window offers a broader scan speed range to achieve the desired surface roughness, relative density, and microhardness values with a laser power of over 200 W. Specifically, concurrently optimizing all part properties within this laser power range appears unfeasible once the scan speed exceeds 1,750 mm/s. Furthermore, the tongue-shaped profile exhibited by the optimal window indicates a loss of optimization capability in the low-power region of the process map. The process was not able to meet all the target criteria below 150 W power, regardless of the scan speed. The shape of the optimal window also confirms that VED is a reliable predictor for surface roughness and relative density only in the high-power region. Despite the VED contour lines in Figure 9 bounding the optimal process window between 100 and 300 J/mm^3 in the first instance, this aggregate parameter cannot capture the complex interaction between laser power and scan speed. Under similar energy density conditions, specific power–speed combinations could not optimize IN725 parts manufactured by PBF-LB/M. In particular, in the low-power region of the process map, parts fabricated under optimal VED values may exhibit a coarse surface texture and microstructure characterized by lack-of-fusion pores. VED was confirmed to be a more precise indicator of microhardness.

Given that hatch spacing and layer thickness were not varied in this study, the process window in Figure 9 remains constrained to the specific combination of 30 μm layer thickness and 50 μm hatch distance. Its applicability to different parameter regimes should therefore be considered with caution.

4. Conclusion

This study optimized the process parameter combinations for PBF-LB/M to manufacture high-quality parts from waste material-derived IN725 alloy. Using recycled powder feedstock further demonstrated the feasibility of sustainable additive manufacturing for high-performance nickel-based superalloys. Experimental surface roughness, relative density, and microhardness measurements were used to train GPR models, considering either laser power and scan speed or VED as input variables. The high predictive accuracy of the models demonstrated the value of data-driven modeling in understanding and optimizing additive manufacturing processes. The promising results of the optimization mark a significant step toward establishing PBF-LB/M as a viable tool for establishing circular economy approaches within industrial practices and applying the process to different nickel-based superalloys. Compared to the prior work of Todaro *et al.*,[24] which was focused on the theoretical validation of IN725 printability, the present work provides a quantitative and application-oriented extension, offering a predictive framework for process control. Key findings include:

(i) The use of laser power and scan speed as separate inputs outperformed VED in predicting surface roughness and relative density. Even when fabricated under the same energy density, parts density and roughness can vary according to the specific combination of laser power and scan speed.

(ii) VED is a more accurate predictor of microhardness, reflecting a stronger correlation between energy input and mechanical properties. However, laser power and scan speed still offer precise point-wise predictions for microhardness when using a GPR model.

(iii) An optimal process window was identified in the laser power–scan speed space to achieve 99.5% relative density, 10 μm surface roughness, and 300 HV microhardness. The wide, tongue-shaped profile of the window underlined the higher sensitivity of the PBF-LB/M process to scan speed, as optimization loss was observed when reducing laser power.

While offering valuable insights and a robust foundation for PBF-LB/M process optimization using recycled IN725, the findings presented in this study represent a preliminary exploratory investigation. Future work should extend the present study by considering hatch distance and layer thickness, as process parameters are expected to influence defect formation and microstructural stability. Future studies could also investigate the effect of heat treatments on the mechanical properties of specimens manufactured with recycled IN725 powder. Furthermore, the modeling framework should be applied to a broader set of mechanical properties, including tensile, fatigue, and creep performance, to comprehensively evaluate recycled IN725 in demanding industrial environments. A comparative study with alternative approaches, including numerical models and other ML algorithms, could also be addressed. Such analyses would provide a clearer perspective on the relative merits and limitations of GPR. Due to its potential and accuracy, GPR offers a powerful tool for optimizing the production of this and other high-performance alloys across different metal additive manufacturing technologies. In this context, developing multi-output GPR models could favor a more holistic investigation of process–structure–property relationships, supporting more integrated optimization strategies.

Acknowledgments

The authors would like to thank Prof. Marco Actis of Politecnico di Torino for supplying the atomized powder used in this study.

Funding

This study was conducted within the MICS (Made in Italy-Circular and Sustainable) Extended Partnership and received funding from the European Union NextGenerationEU (PIANO NAZIONALE DI RIPRESA E RESILIENZA (PNRR)–MISSIONE 4 COMPONENTE 2, INVESTIMENTO 1.3–D.D. 1551.11-10-2022, PE00000004). This manuscript reflects only the authors' views and opinions; neither the European Union nor the European Commission can be considered responsible for them.

Conflict of interest

Mariangela Quarto and Gianluca D'Urso serve as the Editorial Board Members of the journal, but did not in any way involve in the editorial and peer-review process conducted for this paper, directly or indirectly. Other authors declare they have no competing interests.

Author contributions

Conceptualization: Gabriele Locatelli, Sara Bocchi
Data curation: Gabriele Locatelli, Sara Bocchi & Mariangela Quarto
Formal analysis: Gabriele Locatelli
Funding acquisition: Gianluca D'Urso
Investigation: Gabriele Locatelli
Methodology: Gabriele Locatelli, Sara Bocchi
Supervision: Mariangela Quarto Gianluca D'Urso
Writing–original draft: Gabriele Locatelli, Sara Bocchi
Writing–review & editing: Mariangela Quarto Gianluca D'Urso

Ethics approval and consent to participate

Not applicable.

Consent for publication

Not applicable.

Availability of data

Data are available from the corresponding author on reasonable request.

References

1. Reed RC. *The Superalloys*. Cambridge: Cambridge University Press; 2006.

   doi: 10.1017/CBO9780511541285

2. Smith RJ, Lewi GJ, Yates DH. Development and application of nickel alloys in aerospace engineering. *Aircr Eng Aerosp Tech.* 2001;73(2):138-147.

   doi: 10.1108/00022660110694995

3. Pollock TM, Tin S. Nickel-based superalloys for advanced turbine engines: Chemistry, microstructure and properties. *J Propuls Power.* 2006;22(2):361-374.

   doi: 10.2514/1.18239

4. Mali HS, Unune DR. Machinability of nickel-based superalloys: An overview. In: *Reference Module in Materials Science and Materials Engineering*. Netherlands: Elsevier; 2017.

   doi: 10.1016/B978-0-12-803581-8.09817-9

5. Tian Z, Zhang C, Wang D, *et al*. A review on laser powder bed fusion of inconel 625 nickel-based alloy. *Appl Sci.* 2020;10(1):81.

   doi: 10.3390/app10010081

6. Yu H, Zhao Q, Fu J, *et al*. The design of oxidation resistant Ni superalloys for additive manufacturing. *Addit Manuf.* 2025;97:104616.

   doi: 10.1016/j.addma.2024.104616

7. Chowdhury S, Yadaiah N, Prakash C, *et al*. Laser powder bed fusion: A state-of-the-art review of the technology, materials, properties & defects, and numerical modelling. *J Mater Res Technol.* 2022;20:2109-2172.

   doi: 10.1016/j.jmrt.2022.07.121

8. Zhao X, Wang T. Laser powder bed fusion of powder material: A review. *3D Print Addit Manuf.* 2023;10(6):1439-1454.

   doi: 10.1089/3dp.2021.0297

9. Sanchez S, Smith P, Xu Z, *et al*. Powder bed fusion of nickel-based superalloys: A review. *Int J Mach Tools Manuf.* 2021;165:103729.

   doi: 10.1016/j.ijmachtools.2021.103729

10. Kuntoğlu M, Salur E, Gupta MK, *et al*. A review on microstructure, mechanical behavior and post processing of additively manufactured Ni-based superalloys. *Rapid Prototyp J.* 2024;30(9):1890-1910.

    doi: 10.1108/RPJ-10-2023-0380

11. Volpato GM, Tetzlaff U, Fredel MC. A comprehensive literature review on laser powder bed fusion of Inconel superalloys. *Addit Manuf.* 2022;55:102871.

    doi: 10.1016/j.addma.2022.102871

12. Kim KS, Kang TH, Kassner ME, Son KT, Lee KA. High-temperature tensile and high cycle fatigue properties of inconel 625 alloy manufactured by laser powder bed fusion. *Addit Manuf.* 2020;35:101377.

    doi: 10.1016/j.addma.2020.101377

13. Serrano-Munoz I, Fritsch T, Mishurova T, *et al*. On the interplay of microstructure and residual stress in LPBF IN718. *J Mater Sci.* 2021;56(9):5845-5867.

    doi: 10.1007/s10853-020-05553-y

14. Song W, Yang J, Liang J, *et al*. A new approach to design

advanced superalloys for additive manufacturing. *Addit Manuf.* 2024;84:104098.

doi: 10.1016/j.addma.2024.104098

15. Enrique PD, Minasyan T, Toyserkani E. Laser powder bed fusion of difficult-to-print γ' Ni-based superalloys: A review of processing approaches, properties, and remaining challenges. *Addit Manuf.* 2025;106:104811.

doi: 10.1016/j.addma.2025.104811

16. Jena A, Atabay SE, Brochu M. Microstructure and mechanical properties of crack-free Inconel 738 fabricated by laser powder bed fusion. *Mater Sci Eng A.* 2022;850:143524.

doi: 10.1016/j.msea.2022.143524

17. Hu P, Liu Z, Zhang H, Li Y, Zhou Q, Xie J. Effect of remelting on cracking of Inconel 939 fabricated via laser powder bed fusion. *Mater Charact.* 2024;214:114087.

doi: 10.1016/J.MATCHAR.2024.114087

18. Wang Y, Li S, Ma R, *et al.* The effect of laser power on the microstructure and mechanical properties of LPBF Hastelloy X in as-built and heat-treated states. *Mater Charact.* 2025;227:115320.

doi: 10.1016/J.MATCHAR.2025.115320

19. Kenevisi MS, Martelli PA, Titonel I, Bassini E, Marchese G, Ugues D. The effect of solution annealing on additively manufactured and hot isostatically pressed René 80 Ni-based superalloy. *J Mater Res Technol.* 2024;33:6591-6600.

doi: 10.1016/j.jmrt.2024.11.003

20. Xi X, Lin D, Song X, *et al. In-situ* remelting induced healing of cracks and strength-ductility synergy in additively manufactured Haynes 230 alloy. *Addit Manuf.* 2025;98:104638.

doi: 10.1016/j.addma.2025.104638

21. Vilaro T, Colin C, Bartout JD, Nazé L, Sennour M. Microstructural and mechanical approaches of the selective laser melting process applied to a nickel-base superalloy. *Mater Sci Eng A.* 2012;534:446-451.

doi: 10.1016/j.msea.2011.11.092

22. Shoemaker LE. Alloys 625 and 725: Trends in properties and applications. In: *Conference. Superalloys 718, 625, 706 and Various Derivatives (2005).* TMS; 2005. p. 409-418.

doi: 10.7449/2005/Superalloys_2005_409_418

23. Sriwongsa K, Sirimongkolchaikul J, Sukrasorn C, *et al.* Radiation and fast neutron shielding properties of nickel-based superalloys: Inconel 600, 718 and 725 superalloys. *Integr Ferroelectr.* 2022;224(1):120-133.

doi: 10.1080/10584587.2022.2035602

24. Todaro CJ, Rashidi M, Liu RL, *et al.* Laser powder bed fusion of high-strength and corrosion-resistant Inconel alloy 725. *Mater Charact.* 2022;194:112454.

doi: 10.1016/j.matchar.2022.112454

25. Chia HY, Wu J, Wang X, Yan W. Process parameter optimization of metal additive manufacturing: A review and outlook. *J Mater Inform.* 2022;2(3):16.

doi: 10.20517/jmi.2022.18

26. Liu Q, Chen W, Yakubov V, Kruzic JJ, Wang CH, Li X. Interpretable machine learning approach for exploring process-structure-property relationships in metal additive manufacturing. *Addit Manuf.* 2024;85:104187.

doi: 10.1016/j.addma.2024.104187

27. Benedetti M, Perini M, Vanazzi M, Giorgini A, Macoretta G, Menapace C. Atomized scrap powder feedstock for sustainable Inconel 718 additive manufacturing via LPBF: A study of static and fatigue properties. *Prog Addit Manuf.* 2024;9(6):1843-1856.

doi: 10.1007/s40964-023-00547-z

28. Jelinski LW, Graedel TE, Laudise RA, McCall DW, Patel CK. Industrial ecology: Concepts and approaches. *Proc Natl Acad Sci USA.* 1992;89(3):793-797.

doi: 10.1073/pnas.89.3.793

29. Li J, Wang H. Gaussian processes regression for uncertainty quantification: An introductory tutorial. 2025.

doi: 10.48550/arXiv.2502.03090

30. Manfredi P, Trinchero R. A probabilistic machine learning approach for the uncertainty quantification of electronic circuits based on gaussian process regression. *IEEE Trans Comput Aided Des Integr Circ Syst.* 2022;41(8):2638-2651.

doi: 10.1109/TCAD.2021.3112138

31. Moges T, Ameta G, Witherell P. A review of model inaccuracy and parameter uncertainty in laser powder bed fusion models and simulations. *J Manuf Sci Eng.* 2019;141(4):040801.

doi: 10.1115/1.4042789

32. Lee SH. Optimization of cold metal transfer-based wire arc additive manufacturing processes using gaussian process regression. *Metals.* 2020;10(4):461.

doi: 10.3390/met10040461

33. Li H, Song B, Wang Y, Zhang J, Zhao W, Fang X. Laser powder bed fusion process optimization of CoCrMo alloy assisted by machine-learning. *J Mater Res Technol.* 2024;33:3901-3910.

doi: 10.1016/j.jmrt.2024.10.075

34. Maitra V, Shi J, Lu C. Robust prediction and validation of as-built density of Ti-6Al-4V parts manufactured via selective laser melting using a machine learning approach. *J Manuf Process.* 2022;78:183-201.

doi: 10.1016/j.jmapro.2022.04.020

35. El Hassanin A, Silvestri AT, Napolitano F, Borrelli D,

Caraviello A, Astarita A. Investigation of the laser-related parameters in laser-powder bed fusion of inconel 718-Cu blends at fixed volumetric energy density. *J Manuf Process.* 2023;99:456-468.

doi: 10.1016/j.jmapro.2023.05.068

36. Gobber FS, Priarone PC, Pennacchio A, Actis Grande M. Effect of inert gas pressure on the properties and carbon footprint of UNS S32760 powders made from waste materials by gas atomization. *J Mater Res Technol.* 2024;33:8814-8828.

doi: 10.1016/j.jmrt.2024.11.195

37. ASTM Standard B805-17 2017. *Specification for Precipitation Hardening Nickel Alloys Bar and Wire.* United States: ASTM International. Preprint posted online; 2017.

doi: 10.1520/B0805-06R17E01

38. ASTM Standard F3055-14a 2021. *Specification for Additive Manufacturing Nickel Alloy (UNS N07718) with Powder Bed Fusion*. United States: ASTM International. Preprint posted online; 2021.

doi: 10.1520/F3055-14AR21

39. ASTM Standard B212-25 2025. *Test Method for Apparent Density of Free-Flowing Metal Powders Using the Hall Flowmeter Funnel*. United States: ASTM International. Preprint posted online; 2025.

doi: 10.1520/B0212-25

40. ASTM Standard B213-25 2025. *Test Methods for Flow Rate of Metal Powders Using the Hall Flowmeter Funnel*. United States: ASTM International. Preprint posted online; 2025.

doi: 10.1520/B0213-25

41. King WE, Anderson AT, Ferencz RM, *et al*. Laser powder bed fusion additive manufacturing of metals; physics, computational, and materials challenges. *Appl Phys Rev.* 2015;2(4):041304.

doi: 10.1063/1.4937809

42. Yadroitsev I, Bertrand P, Smurov I. Parametric analysis of the selective laser melting process. *Appl Surf Sci.* 2007;253(19):8064-8069.

doi: 10.1016/J.APSUSC.2007.02.088

43. Kamath C, El-Dasher B, Gallegos GF, King WE, Sisto A. Density of additively-manufactured, 316L SS parts using laser powder-bed fusion at powers up to 400 W. *Int J Adv Manuf Technol.* 2014;74(1-4):65-78.

doi: 10.1007/S00170-014-5954-9/METRICS

44. Chen Z, Wie Z, Wie P, *et al*. Experimental research on selective laser melting AlSi10Mg alloys: Process, densification and performance. *J Mater Eng Perform*. 2017;26(12):5897-5905.

doi: 10.1007/s11665-017-3044-5

45. Tian Y, Tomus D, Rometsch P, Wu X. Influences of processing parameters on surface roughness of Hastelloy X produced by selective laser melting. *Addit Manuf.* 2017;13:103-112.

doi: 10.1016/j.addma.2016.10.010

46. Baldi N, Giorgetti A, Palladino M, Giovannetti I, Arcidiacono G, Citti P. Study on the effect of preheating temperatures on melt pool stability in inconel 718 components processed by laser powder bed fusion. *Metals*. 2023;13(10):1792.

doi: 10.3390/met13101792

47. ASTM Standard E384-22 2022. *Test Method for Microindentation Hardness of Materials.* United States: ASTM International. Preprint posted online; 2022.

doi: 10.1520/E0384-22

48. Locatelli G, Quarto M, D'Urso G, Giardini C. Addressing positional and laser source variability in laser powder bed fusion: A mapping method for quality optimization. *Int J Adv Manuf Technol*. 2025;139:4673-4686.

doi: 10.1007/s00170-025-16196-1

49. Williams CKI. Prediction with Gaussian processes: From linear regression to linear prediction and beyond. In: *Learning in Graphical Models*. Berlin: Springer Netherlands; 1998. p. 599-621.

doi: 10.1007/978-94-011-5014-9_23

50. Yang K, Lu J, Wan W, Zhang G, Hou L. Transfer learning based on sparse Gaussian process for regression. *Inform Sci.* 2022;605:286-300.

doi: 10.1016/j.ins.2022.05.028

51. Aggarwal CC. *Neural Networks and Deep Learning*. Berlin: Springer International Publishing; 2023.

doi: 10.1007/978-3-031-29642-0

52. De Oliveira V, Han Z. On information about covariance parameters in gaussian matérn random fields. *J Agric Biol Environ Stat*. 2022;27(4):690-712.

doi: 10.1007/s13253-022-00510-5

53. Neal RM. *Bayesian Learning for Neural Networks*. Vol. 118. Berlin: Springer New York; 1996.

doi: 10.1007/978-1-4612-0745-0

54. Pan R, Gu M, Wu J. Physics-informed Gaussian process regression of in operando capacitance for carbon supercapacitors. *Energy Adv.* 2023;2(6):843-853.

doi: 10.1039/D3YA00071K

55. Hashemi SH, Torabi F, Tontiwachwuthikul P. Machine learning-driven prediction of CO_2 solubility in brine: A hybrid grey wolf optimizer (GWO)-assisted gaussian process regression (GPR) *Approach Energies*. 2025;18(15):4205.

doi: 10.3390/en18154205

56. Hair JF, Black WC, Babin BJ, Anderson RE. *Multivariate Data Analysis.* London: Pearson Education Limited; 2014.

57. Willmott C, Matsuura K. Advantages of the mean absolute error (MAE) over the root mean square error (RMSE) in assessing average model performance. *Clim Res.* 2005;30:79-82.

doi: 10.3354/cr030079

58. Piriz AR, Cortázar OD, López Cela JJ, Tahir NA. The Rayleigh-Taylor instability. *Am J Phys.* 2006;74(12):1095-1098.

doi: 10.1119/1.2358158

59. Chivel Y. Optical in-process temperature monitoring of selective laser melting. *Phys Procedia.* 2013;41:904-910.

doi: 10.1016/j.phpro.2013.03.165

60. Mannan S, Veltry F. Time-temperature-transformation diagram of alloy 725. In: *Superalloys 718, 625, 706 and Various Derivatives (2001)*. Warrendale: TMS; 2001. p. 345-356.

61. Javidrad HR, Salemi S. Effect of the volume energy density and heat treatment on the defect, microstructure, and hardness of L-PBF inconel 625. *Metall Mater Trans A.* 2020;51(11):5880-5891.

doi: 10.1007/s11661-020-05992-x

62. Capelli A, Cacace S, Semeraro Q. XCT characterization and mechanical properties of Ti6Al4V produced by L-PBF using the same volumetric energy density. Progress in Additive Manufacturing. *Prog Addit Manuf.* 2025;10:4787-4802.

doi: 10.1007/s40964-024-00862-z

63. Wang S, Ning J, Zhu L, *et al.* Role of porosity defects in metal 3D printing: Formation mechanisms, impacts on properties and mitigation strategies. *Mater Today.* 2022;59:133-160.

doi: 10.1016/j.mattod.2022.08.014